Electron Microscopic Tomography: A Tool for Probing the Structure and Function of Subcellular Components

Bruce F. McEwen,[1,2] Amy B. Heagle[1]

[1] Laboratory of Cell Regulation, Wadsworth Center, New York State Department of Health, P.O. Box 509, Albany, NY 12210-0509

[2] Department of Biomedical Sciences, State University of New York, Albany, NY 12222

Received 17 October 1996

ABSTRACT: Tomography is a powerful tool for obtaining three-dimensional information from transmission electron microscopy, but its application faces unique challenges. A single-axis tilt geometry for data collection results in anisotropic resolution because full angular coverage is not feasible for most specimen preparations. This effect can be minimized by combining two single-axis tilt series that have been collected orthogonal to each other. Rapid freezing has been successfully used to preserve the native structure of biological specimens in a form that can be visualized in the high-vacuum environment required for electron microscopy; however, these preparations are extremely labile to electron exposure. As a result, application of tomography to frozen-hydrated specimens has only recently become feasible with the development of automatic data collection, and with a renewed appreciation for the principle of dose fractionation. Even with the limitations of traditional specimen preparations and conventional methods of data collection, electron microscopic tomography has been successfully employed to probe the structure and function of several important cellular components. Current efforts include combining electron microscopic tomography and video-enhanced light microscopy to correlate ultrastructural variation with the direction of chromosome motion during mitosis. Int J Imaging Syst Technol, **8,** 175–187, 1997

Key words: electron microscopy; tomography; mitosis; kinetochore; image analysis

I. INTRODUCTION

Tomography is a method for reconstructing a three-dimensional (3D) volume from a set of 2D projections, using the Radon transformation. The concept was originally formulated by Bracewell [1,2], and introduced to electron microscopy by Hoppe [3] and by De Rosier et al. [4,5]. The term *tomography* literally means visualization of slices, which, in the strict sense, is only applicable when the data have been collected via a single-axis rotation geometry. Although single-axis data collection is standard in biomedical imaging (e.g., CAT scan, scanning via computerized axial tomography), other data collection geometries are also routinely used.

In the last 10 years, electron tomography has proved to be an effective tool for 3D structure–function determination in cellular and molecular biology (reviewed in [6–8]). Recent successful applications include determining the location of microtubule initiation sites in centrosomes isolated from fruit fly embryos [9], demonstrating dynamic changes that occur in muscle *Z* bands with contraction [10], characterizing the arrangement and morphology of crystals formed during the initial events of bone formation [11,12], and providing new insight into the folding of DNA into chromosomes [13,14]. Here we briefly review the methodology, including recent efforts to overcome radiation damage and an unfavorable specimen geometry, and present a new application where electron tomography is combined with video-enhanced light microscopy to correlate structural determination with motion.

A. Image Formation in Electron Microscopy. Electron tomography is based on the assumption that input images are true projections of the original object, and therefore, it is crucial to consider the conditions under which this assumption is valid. In transmission electron microscopy, images are formed by passing a beam of electrons through the specimen. Although electrons exhibit wave motion, unlike photons, they are also charged particles. As a result, incident electrons passing close to an atomic nucleus experience the effects of a strong electric field and are deflected from their original path without losing energy (elastic scattering). On the other hand, incident electrons passing close to specimen electrons are deflected with a loss of energy to the specimen (inelastic scattering) [Fig. 1(a)].

Although absorption of incident electrons is rare for most specimens, an analogous form of contrast known as amplitude contrast is created by use of an objective aperture that prevents electrons that have been scattered at a wide angle from being included in the image formation [Fig. 1(b)]. The number of

Correspondence to: B. F. McEwen

Contract grant sponsor: National Science Foundation; *Contract grant numbers:* MCB 9420772, BIR 921904

Contract grant sponsor: National Institutes of Health; *Contract grant numbers:* GMS 40198, NCRRBTP P41-01219

 CCC 0899–9457/97/020175-13

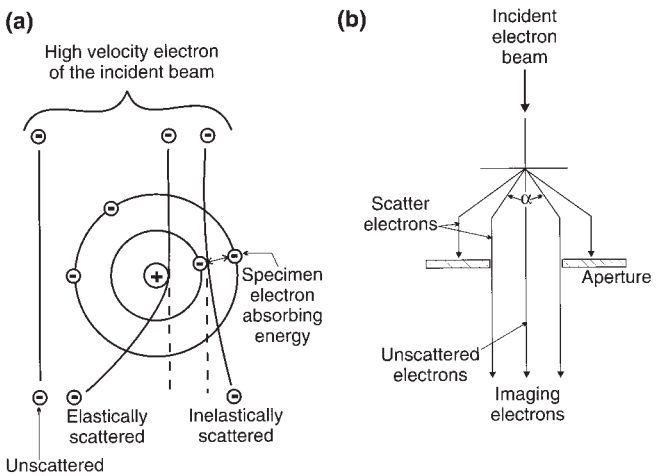

Figure 1. Image formation in transmission electron microscopy. (a) Electron scatter. Most electrons in the incident beam suffer one of three fates upon interaction with the specimen. Owing to the high energy of the beam, a significant fraction passes through the specimen without any interaction (i.e., is unscattered), particularly in regions of low specimen mass. Incident electrons that pass close to the nucleus of a specimen atom are scattered but without losing energy (elastic scattering), because of the large mass difference between electrons and atomic nuclei. Incident electrons that pass close to specimen electrons are scattered with a loss of energy to the specimen electrons (inelastic scattering). For specimens stained with heavy metals, where amplitude contrast predominates [see (b)], both elastic and inelastic scattering contribute to image formation. Only elastic scattering, however, contributes to image formation for unstained specimens, where phase contrast predominates. (b) Contrast formation. Amplitude contrast is generated because widely scattered electrons are blocked by the objective aperture and removed from the beam. Wide-angle scattering is prevalent in areas of stained specimens with high concentrations of heavy-metal stain. Phase contrast is generated in low-angle scattering by a phase shift between scattered and unscattered electrons. (Adapted from [62]).

electrons that pass through the acceptance angle of the objective aperture is directly related to the negative logarithm of the total specimen density along the path of the electrons:

$$n = n_0 \exp\{-N\sigma(\alpha)\mu\}$$

where n = number of electrons; α = acceptance angle of the objective aperture; $\sigma(\alpha)$ = the scattering cross section; N = Avogadro's number; and μ = mass thickness (i.e., product of density and thickness) [15]. This relationship holds for elastic and inelastically scattered electrons, but is no longer valid if a significant portion of the electrons experience more than one scattering event. Therefore, if multiple scattering events are rare, amplitude contrast records the projection density of the specimen. To prevent multiple scattering, thin specimens and high electron-accelerating voltages are standard in electron microscopy. Conventional instruments use accelerating voltages up to 120 kV and are usually capable of providing quality images for specimens up to 0.12–0.15 μm thick. Special intermediate (200–400 kV) and high ($\geq$1 MV) voltage instruments are employed to view specimens in thickness ranges of 0.15–0.50, and 0.20 to several microns. The exact thickness limit before significant multiple scattering occurs depends upon the specimen composition and is therefore hard to predict in advance, although rough calculations can be made [15].

The magnitude of electron scattering depends upon the atomic number of the atoms in the specimen. Biological material is primarily composed of light atoms such as carbon, nitrogen, and oxygen, which are weak scatterers. In addition, the media in which specimens are embedded (plastic, ice, etc.) are dominated by the same light atoms. For this reason, it is common practice to stain specimens with solutions of heavy metals such as lead, osmium, and uranium, to provide amplitude contrast between the specimen and the background.

Despite the success of heavy-metal staining in providing strong contrast for a wide variety of biological specimens, high-resolution structural determinations generally employ unstained specimens because of the limited capacity of stain atoms to bind uniformly to the specimen surface, and penetrate into fine crevices. For unstained specimens and thin-stained specimens ($\lesssim$0.030 nm), image formation is primarily generated by phase contrast. Phase contrast provides a projection of specimen mass density if the accelerating voltage is sufficient. Special care is also required to insure that the phase-shift information emerging from the specimen is accurately converted into amplitude variations in the recorded images. This in turn requires the specimen atoms to be weak scatterers, the beam convergence and energy spread to be small, and the objective defocus to be an appropriate value. For phase contrast, inelastic scattering contributes to the background noise in the image, and hence the signal can be improved by energy filtration [16]. For resolutions higher than 1.5–2.0 nm, a large number of other technical considerations must also be addressed such as the contrast transfer function of the electron beam and specimen drift [17].

B. Data Collection and Computation of the 3D Reconstruction. The requisite views for a 3D reconstruction via electron tomography are obtained by tilting the specimen in a fixed electron beam, in contrast to medical imaging, where the patient is in a fixed position while the source-detector arrangement is rotated. The reason for tilting the specimen is that the specimen is small, typically mounted on a grid a few millimeters in diameter, while the electron microscope is relatively large and immobile.

The number of views required for a tomographic reconstruction is determined by the desired resolution:

$$d = \alpha D/N$$

where d = resolution; D = effective diameter of the object [18]; α = the total angular range; and N = number of projections collected. Ideally, α should be π radians, but generally it is limited to about $2\pi/3$ radians. Typically images are collected in 2° angular increments (i.e., N = 61 views over a 120° angular range). Each view is recorded either on film or on a CCD camera that is coupled to a YAG scintillator via fiber optics. A CCD camera provides direct digital recording, while an additional digitization step is required if film is used. In either case, the 3D reconstruction is computed off-line after data collection is complete, owing to the time required for data collection and the necessity for further alignment.

Specimen stages used for transmission electron microscopy

are not perfectly eucentric relative to the high resolution obtained, and therefore, it is necessary to translate and refocus the specimen as the tilt angle is incremented. Focus adjustment is accompanied by specimen rotation and change of magnification. In addition, only the approximate direction of the tilt axis is known during data collection. Thus, one must determine the tilt-axis direction, rotationally and translationally align the data set, and correct for scale changes before computing a 3D reconstruction. The most common alignment scheme used in electron tomography is to place colloidal gold particles on the specimen surface before recording the tilt series. Owing to their relatively small size and high mass density, the gold particles serve as localized points that can be viewed throughout the tilt series and used as fiduciary markers. Alignment parameters are computed from the coordinates of 10–20 markers identified in every view of the tilt-series:

$$P_i\mathbf{x}^j = R_i s_i \mathbf{p}_i^j + \mathbf{d}_i$$

where P_i = the projection matrix for the ith tilt angle; $\mathbf{x}^j$ = the coordinates of the jth marker in 3D space; R_i = the rotation matrix of the ith projection around the axis orthogonal to the image plane; s_i = the scale; $\mathbf{p}_i^j$ = the measured coordinates of the jth marker on the ith projection; and $\mathbf{d}_i$ = the translation of the ith marker. Conjugate gradient methods [19–21] or closed-form solutions [22] are used iteratively to minimize computed and measured values of $P_i\mathbf{x}^j$ for all values of i and j.

Computation of the 3D reconstruction from an aligned data set can be accomplished via Fourier, iterative real-space, or modified back-projection methods, with the latter having the advantage of computational efficiency [18,23]. The real-space methods (i.e., iterative and modified back-projection) are based upon the concept of back-projection where $p'_{i,\theta}$, a value that is associated with the contents of the ith pixel, $p_{i,\theta}$, is distributed along a corresponding ray so that the contents of each voxel falling within the ith ray receive an equal share (i.e., $p'_{i,\theta}$ is ''back-projected'' into the reconstruction volume). This is illustrated for three projections in Figure 2. In the modified back-projection approach, the back-projected quantity is the convolution of the jth projection, $p_{\theta j}$, with a function, f_j, that compensates for the over sampling of low-resolution components in the data set:

$$p'_{\theta j} = p_{\theta j} \circ f_j$$

where θ is the tilt angle of the jth projection. It is convenient to compute the weighting function in Fourier space where, according to the convolution theorem,

$$P'_{u,\theta} = P_{u,\theta} F_u$$

where the capital letters refer to the Fourier transforms of the corresponding real-space functions and u is the spatial frequency. The modified data set is then converted back to real space for the back-projection computation [18,23]. The latter is accomplished by creating ''back-projection rays,'' $P_j^b(x^j, y^j, z^j)$, via convolution of $p'_{\theta j}(x^j, y^j)$ with the function:

$$1_j = \delta(x^j, y^j) \cdot c(z^j)$$

where j denotes the jth tilt angle, θ; and

$$c(z^j) = 1 \text{ for } -a \le z^j \le a$$
$$c(z^j) = 0 \text{ otherwise}$$

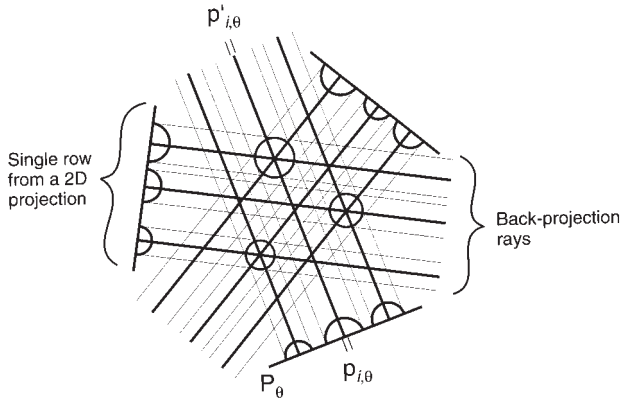

Figure 2. Illustration of the back-projection algorithm for tomographic reconstruction. Single rows from three different projections in a recorded tilt series are represented by lines with domelike structures. The latter indicate image features corresponding to high mass density in the original structure. Lines emanating from each projection represent back-projection rays. One of the projections and its set of back-projection rays are labeled. For another projection, P_θ, the contents of a single pixel, $p_{i,\theta}$, and its corresponding back-projection ray, $p'_{i,\theta}$, are indicated. Back-projection rays arising from the domelike structures intersect in the 3D reconstruction volume at the locations corresponding to points of high mass density in the original structure. (Reproduced from [63], with permission).

In practice, $2a$ is chosen to be larger than the object diameter, D. Thus:

$$P_j^b(x^j, y^j, z^j) = p'_{\theta j}(x^j, y^j) \circ 1_j(x^j, y^j, z^j)$$

and the 3D reconstruction becomes:

$$b(x^j, y^j, z^j) = \sum_j P_j^b(x^j, y^j, z^j)$$

A qualitative illustration of the method is given in Figure 2, where back-projection rays from the three high-density regions of three projections intersect in the reconstruction volume at points corresponding to the locations of the objects in the specimen that gave rise to the projection densities. In this fashion, the mass density of the original specimen is reconstructed.

C. Minimizing Electron Dose. Electron microscopes must operate at high vacuum to prevent scattering of the incident electron beam by air molecules along the optical path. For this reason, specimens have traditionally been dehydrated, embedded in a plastic resin, cut into thin sections, and stained with heavy metals before viewing. Alternatively, specimens can be placed in a solution of heavy metal stain that dries down into a glasslike film. Since these preparations are relatively beam stable, minimizing electron dose has not been a major concern in electron tomography. Unfortunately, traditional methods for specimen preparation are highly disruptive to some specimens, and in all cases, high-resolution fine structure is distorted. Development of cryoelectron microscopic techniques [24,25] has enabled viewing unstained specimens in their native, hydrated state, but these preparations are beam labile. Until recently, beam lability has limited cryoapplications to specimens containing multiple copies of a structural

Table I. Predicted resolution for beam-labile specimens.

Volume	D (nm)	N	Q e/nm^2	d_p (nm)	d_v (nm)
Without dose fractionation					
1	521	61	82	18.2	18.2
2	285	41	122	14.9	14.9
3	133	25	200	11.6	11.6
4	48	13	385	8.4	8.4
With dose fractionation					
1	521	241	21	35.9	4.6
2	285	121	41	25.7	5.0
3	133	51	82	18.2	4.6
4	48	25	200	11.6	4.2

Expected resolution levels are shown that are feasible for four different-sized specimens. D = specimen diameter; N = number of views collected over ±120° angular range; Q = electron dose per projection (Q_{total} for the reconstruction ≃ 5000 e/nm^2); d_p = statistically significant resolution of each projection image; and d_v = resolution of the reconstructed volume as limited by angular sampling. According to the principle of dose fractionation, the statistically significant resolution of the reconstructed volume is determined by Q_{total}, rather than Q, and is equal to 2.3 nm for all examples.

motif because different copies of the unit structure can be averaged and used to provide different tilt views.

Recently, the development of methods for automated data collection [26–28] has enabled the recording of a tilt series at a greatly reduced electron dose, resulting in the application of cryoelectron tomography to small model systems [29,30]. This development has regenerated interest in determining the minimum electron dose required for adequate signal-to-noise ratio (S/N) in electron tomography. The image signal in an average unit area is given by:

$$S = I_0 d^2 C$$

where I_0 = the illumination level (i.e., the electron dose); d = limiting resolution; and C = ''contrast,'' a quantity related to image variance. Assuming noise follows a Poisson distribution:

$$N = (I_0 d^2)^{1/2}$$

and

$$S^2/N^2 = I_0 d^2 C^2 \geq 25$$

The requirement for $S/N \geq 5$ is an empirical rule of thumb known as the Rose criteria [31]. The value of C varies with the specimen, but for a mass density 1.2 times that of water, which is reasonable for unstained specimens, Saxberg and Saxton [32] calculated that 3000 e/nm^2 are required for statistical significance at 3 nm resolution (thus, $C \sim 0.03$ for this density). The upper radiation limit before severe specimen damage (i.e., the specimen starts to ''bubble'') is about 5000 e/nm^2. In theory, it is possible to obtain 2.3 nm resolution with this maximum dose, but specimens suffer increasing loss of high-resolution features with dose levels much above 1000 e/nm^2 [33]. Thus, the dose requirement for statistical significance is in conflict with minimizing resolution loss due to radiation damage. Although no quantitative measure of resolution loss with electron exposure has been formulated, empirical data suggest that 3–4 nm is the resolution limit for a 2D image of a single copy of a frozen-hydrated specimen [33].

Since radiation damage appears to be cumulative, the dose per image must be lowered in proportion to the number of images in the tilt series. Thus, resolution in tomographic 3D reconstructions appears to be constrained by the conflicting demands for lower dose to prevent specimen damage, higher dose for adequate S/N, and more tilt views for adequate angular sampling. Table I lists resolution values that are possible for various sized objects if S/N and the angular sampling are matched to the same resolution level.

The values in the first half of Table I were computed assuming that the desired level of resolution must be obtained for each image of the tilt series. Hegerl and Hoppe, however, postulated that the required dose can be fractionated among different views in the tilt series [34]. Analyzing projection formation as a stochastic process, Hegerl and Hoppe showed that:

$$\text{Var}\{P(x, \theta_k)\} = (2/Q)R_{\max}$$

and

$$\text{Var}\{\rho(r, \phi)\} = (2\pi^2/3KQ)R_{\max}^3$$

where $\text{Var}\{P(x, \theta_k)\}$ and $\text{Var}\{\rho(r, \phi)\}$ = variances of the projection and object functions expressed in polar coordinates; Q = integral dose per projection; $R_{\max}$ = Fourier radius of the limiting resolution; and K = number of projections (over the full 180° angular range). If Q_T is the total dose required for statistical significance in an image (i.e., $S/N \geq 5$), then the minimum dose per projection required for statistical significance in the 3D reconstruction is approximately Q_T/K. This result indicates that a statistically significant 3D reconstruction can be computed from statistically insignificant projections, and that in principle, the required electron dose can be partitioned among any number of projections. This controversial theorem has recently been verified by McEwen et al. [31] using an extensive series of computer simulations (Fig. 3). The practical importance of dose fractionation is that beam lability does not prevent adequate angular sampling. Therefore, in principle it should always be possible to obtain 3–4 nm resolution via cryoelectron tomography. The second half of Table I demonstrates that using dose fractionation, 4–5 nm can be obtained for most specimens using a reasonable number of tilt views. With this level of dose fractionation, individual projections receive adequate dose for alignment because a sufficient number of low-resolution features are imaged with statistical significance [31]. Presumably, the principle of dose fractionation will be useful in other applications of biomedical imaging where the total radiation exposure is a concern.

D. Specimen Geometry and the Resulting Limited Angular Coverage. Most specimens currently studied by electron to-

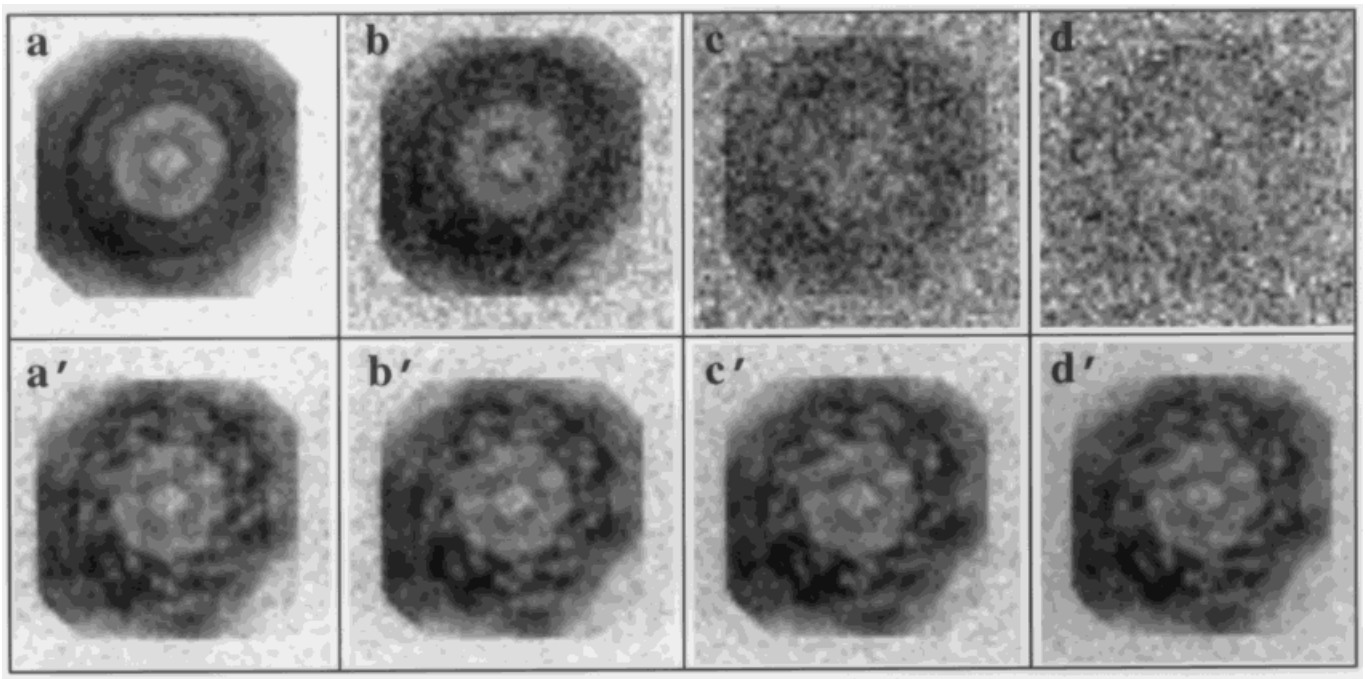

Figure 3. Simulation of dose fractionation. In a computer simulation, a total dose of 9×10^6 quanta/pixel has been fractionated among 36, 180, 1800, and 18,000 projections. All projections were computed from a 3D helical model created by stacking rotated copies of a 2D electron microscopic image of a centriole. Frames (a–d) show the zero-degree projections imaged at the fractionated dose, and frames (a′–d′) show the central slice from the corresponding 3D reconstructions. The image quality of the 3D reconstructions remains roughly constant, despite the extreme degradation of individual projections with increased dose-fractionation. (Taken from [31], with permission).

mography, whether frozen-hydrated, dried down from stain solution, or embedded in plastic and cut into thin sections, have planar dimensions of 100–300 μm, but thicknesses of 0.05–0.50 μm. Thus, the specimen geometry is effectively an infinite slab (Fig. 4). This has several deleterious consequences for electron tomography, the most significant of which is the limited angular coverage ($\pm 60° - \pm 70°$) that arises because the specimen becomes impenetrable to the electron beam at high tilt angles. As a result, electron tomographic reconstructions computed from a single-axis data set have a wedge of information missing in their 3D Fourier transforms (Fig. 5). In general, missing Fourier information along one axis leads to an elongation of the specimen in real space and anisotropic resolution (i.e., different along each of the three coordinate axes) [22,23]. This in turn causes linear features in the cell (membranes, fibers, etc.) to appear discontinuous when oriented in an unfavorable direction.

One solution to the missing-wedge problem is to mount specimens in a cylindrical geometry, since the full angular range will be available if the specimen is tilted about the cylindrical axis. This approach has been successfully employed on material mounted inside or on the surface of a micropipette [35], but the method has not yet seen general use owing to difficulties in mounting specimens in or on the micropipette. Alternatively, the effects of anisotropic resolution can be mitigated by employing a conical geometry for collecting the tilt series, because this scheme reduces the amount of missing Fourier information from a wedge to a cone (Fig. 5) [23]. For electron tomography, however, conical tilting requires more views for the equivalent resolution and is difficult to implement on commonly available tilt-rotation stages because the sample cannot be easily maintained at the eucentric point.

Recently, Penczek et al. [22] developed a double-tilt scheme that combines two single-axis data sets that are collected about orthogonal tilt axes. This scheme, which is readily implemented on existing specimen stages of electron microscopes, reduces the amount of missing Fourier information from a wedge to a pyramid, and thereby provides most of the benefits of conical tilting. Test 3D reconstructions of a mitochondrion demonstrate that the double-tilt scheme prevents membrane discontinuities and results in higher clarity of fine structure [22]. As with conical tilting, double tilting requires collecting twice the amount of data, but Penczek et al. demonstrated that the benefits of double tilting could be realized without increasing the number of views and with only a small loss of resolution, by using a finer tilt-angle increment at high tilt angles and a coarser tilt-angle increment at low tilt angles. It will be important to test whether the principle of dose fractionation can be applied to the double-tilt scheme, and thereby enable collecting a double-tilt series at the same total dose and S/N as a single-axis series.

E. Application of Electron Tomography to Chromosome Motion. We have initiated a study of chromosome motion that combines electron tomography with video-enhanced light microscopy. Since electron microscopy is incompatible with living systems, light microscopy is required to study motion of cellular components. To retain high-resolution structural determinations, same-cell correlative light and electron microscopy techniques have evolved. In this approach, cells are followed from a living

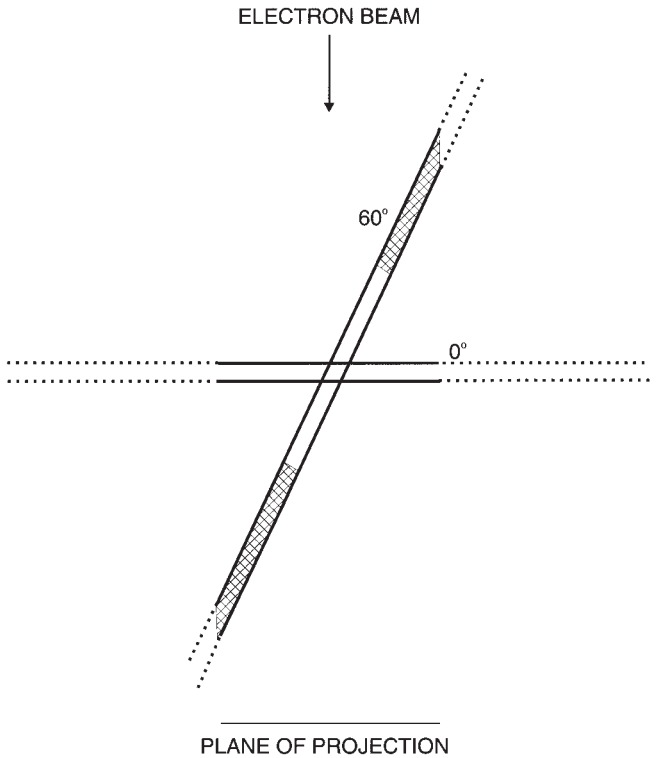

Figure 4. Illustration of the infinite-slab geometry typical of electron microscopic specimens. Arrow indicates the direction of the electron beam, while the plane of projection indicates the area where the image is recorded. The direction of the tilt axis is orthogonal to the plane of the figure. The solid lines indicate the region of the specimen that is in the viewing area at the indicated tilt angles. Hatched area of the specimen denotes material that is in the viewing area at 60° tilt but not at 0° tilt. This material causes a problem only in areas of the specimen where the electron beam passes through both hatched and clear regions. This area of overlap is small as long as the tilt angle is not $>60°$, and the length of the viewing area is 5–10 times the specimen thickness, as in the illustration. If the length of the viewing area and specimen thickness are more nearly equal, then a significant portion of the 3D reconstruction will be affected by the artifact. Above 60°, the area of overlap increases rapidly with increased tilt angle, as does the path length of the electron beam. For these reasons, quality data are rarely obtained above 70° tilt.

state by light microscopy, rapidly fixed at a defined point in time, and then viewed in high resolution by electron microscopy. In the following study, we have incorporated electron tomography into this process for high-resolution 3D analysis.

The elegant movements of chromosomes during mitosis have long fascinated biologists, even before the significance of this phenomenon for genetic segregation was appreciated. In vertebrates, the process begins with the disassembly of cytoplasmic microtubules, condensation of the replicated DNA into chromosomes, and breakdown of the nuclear envelope [36]. The microtubular network re-forms as a bipolar spindle with the fast growing (+) end of each microtubule distal to the spindle pole from which it emanates (Fig. 6). Mitotic chromosomes consist of duplicate sister chromatids that are held together at a point on the chromosome known as the primary constriction. Chromosomes become attached to the spindle when sister chromatids bind microtubules from opposite poles. Usually a chromosome is initially mono-oriented but, with rare exceptions, it eventually acquires bi-oriented attachment. In a process known as congression, bi-oriented chromosomes migrate to the spindle equator, where they are positioned halfway between the two poles. The stage when all chromosomes have migrated to the equator is known as metaphase, and it is characterized by oscillations of many of the chromosomes about the equatorial plane. Metaphase is followed by anaphase, where sister chromatids separate and migrate independently toward their respective spindle poles. Upon completion of anaphase, chromosomes decondense, the nuclear envelope reforms, and the process of cytokinesis creates two distinct cells.

Chromosome movement during mitosis results from an interaction between the kinetochore, a specialized microtubule-binding region of each chromatid, and the (+) ends of a subset of spindle microtubules known as the kinetochore microtubules (kMts). The kinetochore consists of a trilaminar disk (a densely staining outer plate separated from a densely staining inner plate by a lightly staining region) with fibrous material on the distal surface of the outer plate (Figs. 6 and 7) [37]. Several proteins have been localized to the kinetochore area but none conclusively to the outer plate [38,39]. According to our current understanding, the kinetochore is a functionally complex organelle that produces force for poleward chromosome motion [40–43] while simultaneously holding the ends of kMts and allowing them to grow and shrink by addition or loss of subunits within its confines [44–46].

From initial attachment through early anaphase, kinetochores are capable of accommodating both poleward (P) and away from the pole (AP) motion [43]. Each type of movement is distinct, with P motion requiring kMt disassembly and movement toward kMt (−) ends, and AP motion requiring kMt assembly and movement toward kMt (+) ends [43,47–49]. The direction of chromosome motion abruptly switches throughout most of mitosis, with oscillations especially evident during monopolar attachment and metaphase [43,50].

Presently there are no direct data concerning the molecular events involved in P and AP chromosome motion, or the switching mechanism. One model proposes that during AP motion the kMts grow through the outer plate to reach an internally located (+) end directed microtubule motor protein, while during P motion force is generated from the energetics of kMt disassembly at the distal surface of the outer plate where kMts are anchored by corona fibers [47,51,52]. A variety of data have subsequently demonstrated that tension on the kinetochore/kMt junction is a primary effector for switching kinetochores from P to AP motion [49]. In addition, more recent data indicate that the kinetochore switches between a force-generating phase for P motion and a neutral state [50,53], and does not normally generate AP motion. These recent observations suggest to us a model in which it is the force for P motion, rather than AP motion, that is generated internally. Tension pulls the kMts out to the distal surface of the outer plate, thereby disengaging the force-generating mechanism and creating the neutral state. This model is illustrated by the position of kMt ends in Figure 7. These two contrasting models for microtubule involvement in switching the direction of motion can be tested by measuring the depth of kMt penetration during P and AP motion.

Here we present the penetration data obtained by combining electron tomography with video-enhanced light microscopy. In this approach, cells are followed in a living state by light microscopy, rapidly fixed at a point in time when the direction of motion

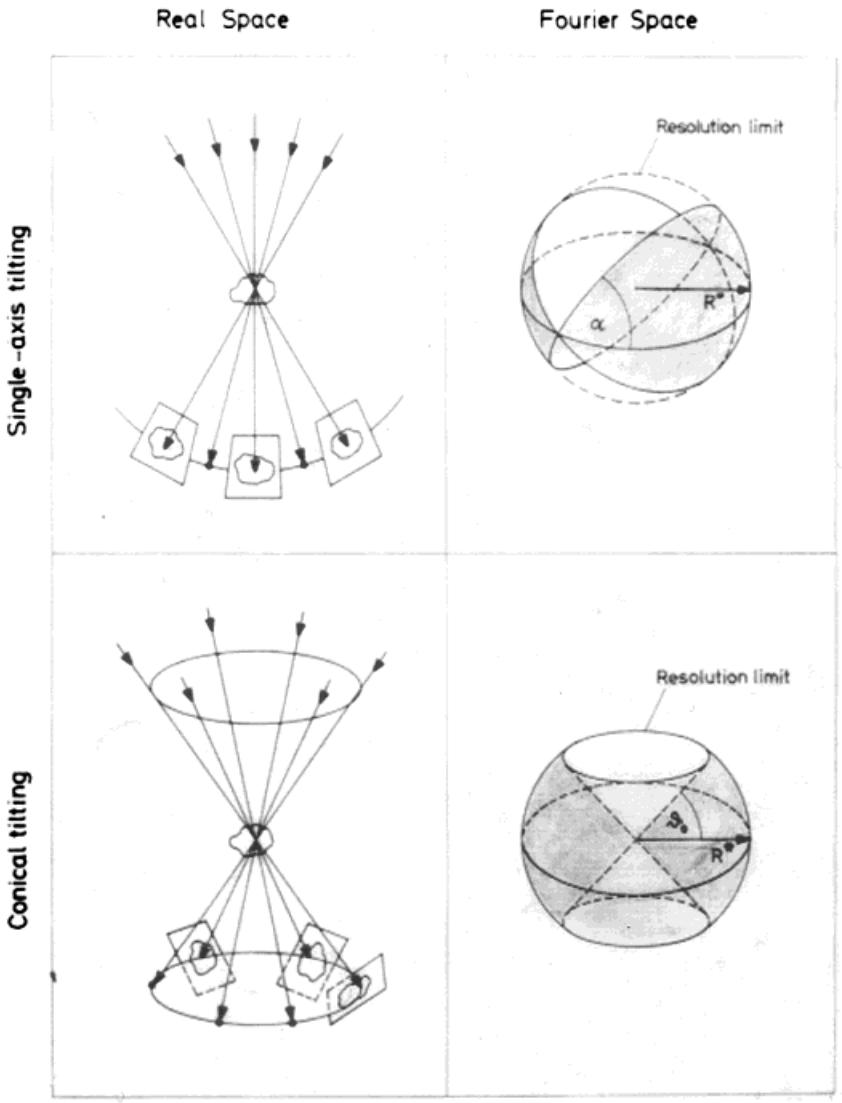

Figure 5. Illustration of the missing information for single-axis and conical tilting. The tilting geometries are shown in real and Fourier space. The Fourier transform of each 2D projection is a central slice in the 3D Fourier transform, and as a result, projections from the tilt series sample the Fourier transform in the shaded regions. The 3D Fourier transforms contain an unsampled region that is a wedge for single-axis tilting and a cone for conical tilting. R^* is the Fourier radius of limiting resolution, beyond which the transform is undersampled. R^* can be increased by using the smaller tilt-angle interval between successive projections. The maximum tilt angle is indicated by α in the single axis and by ϑ in the conical. (Reproduced from [63], with permission).

is well defined, and the location of kMt (+) ends determined via electron tomography. Thus far, our results show no correlation between direction of motion and depth of kMt penetration, indicating that neither switching model is correct.

II. EXPERIMENTAL METHODS

PtK_1 cells were grown on glass coverslips and transferred to microperfusion chambers for video-enhanced light microscopy [54,55]. Chromosome motion was recorded via time-lapse video, using differential interference contrast, on a Nikon Microphot, with a 60× objective [55]. The recording rate was 15 frames/min, and the culture was maintained at 37°C using a block heater for the specimen stage. At the appropriate time, cells were rapidly fixed by perfusion with 2.5% glutaraldehyde in 0.1 M phosphate buffer. Fixation was verified by continuing the video recording. As observed by Rieder and Alexander [54], all motion ceased within 1–2 s after the fixative reached the cell. Single low-magnification frames were recorded and the position of the filmed cell was marked on the glass coverslip with an objective scribe. Coverslips were then transferred to small chambers and further fixed for a total of 30 min in 2.5% glutaraldehyde, washed with phosphate buffer, and postfixed with 2% OsO_4. Specimens were treated with 0.15% tannic acid and stained for 60 min with 1% uranyl acetate. This preliminary staining was followed by a graded ethanol dehydration series, extraction with propylene oxide, and flat embedding in epon [56]. After curing, scribe marks were transferred to the epon, the glass coverslips removed by etching, and the resulting preparations trimmed and glued onto

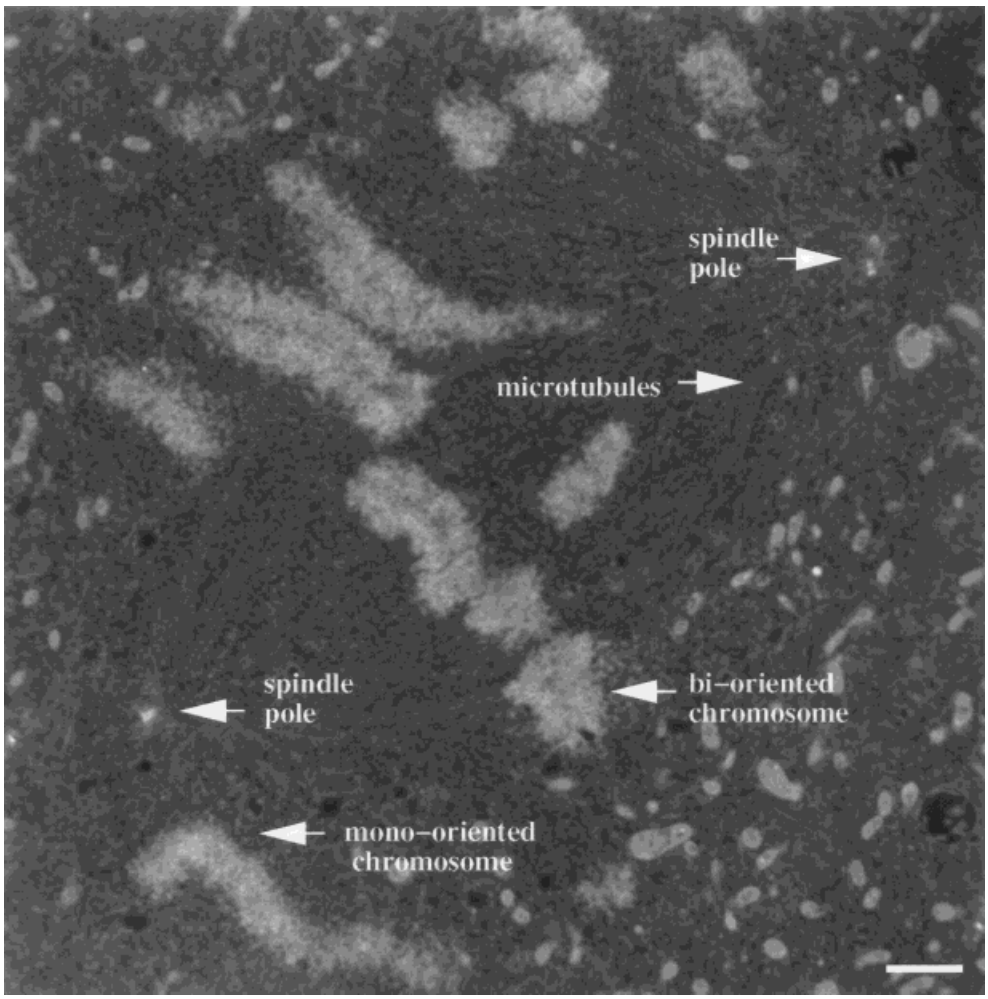

Figure 6. Overview of a mitotic cell. An electron micrograph from the cell displaying the spindle poles, microtubules, and chromosomes. The indicated bi-oriented chromosome is connected to both spindle poles via microtubules attached to the sister kinetochores while the indicated mono-oriented chromosome still has one kinetochore that is unattached to the mitotic spindle. Bar = 2 μm.

an epon block for sectioning [54]. Serial sections approximately 130 nm thick were collected on formvar-coated slot grids, and subsequently stained with uranyl acetate and lead citrate.

Successive serial sections were viewed on a Zeiss 910 electron microscope, using an accelerating voltage of 120 kV, an LaB_6 filament, and the Köhler illumination system. Collection of the double-tilt series proceeded by successively collecting two single-axis tilt series, one orthogonal to the other (Fig. 8). For each series, the specimen was tilted about a single axis, orthogonal to the electron beam, in 2° intervals from −60° to +60°. After collection of the first series, the specimen was removed from the microscope and rotated manually by approximately 90°. Each projection was digitally recorded using a CCD camera coupled with a fiberoptic YAG crystal (Gatan Corp., CA).

All image manipulation and image processing were carried out on a Silicon Graphics INDY using SPIDER/WEB, a modular image processing/graphics display software system [57], and Sterecon, a graphics package [58]. The first step is alignment of projections within each single-axis series, which was accomplished by selecting reference points common to all projections using the method of Penczek and Feuerbach [22]. Ten to 12 gold particles encompassing the kinetochore region were manually selected using the WEB graphics interface for SPIDER. The same gold markers were selected in each projection of the first and second single-axis series. For each projection series, the selected marker coordinates were then subjected to the iterative least-squares analysis. Generally the average error is <1 pixel, demonstrating the reliability of the resulting alignment parameters. These parameters were applied to the physical alignment of the projections. Wrap-around effects in the resulting images show the extent of these adjustments (Fig. 8).

The two orthogonal tilt series were then aligned to one another, in terms of Eulerian angles, using a quaternion-based routine [22]. The resulting Eulerian angles were used as input parameters to compute the 3D reconstruction via the modified back-projection method. However, in this case a general weighting function must be employed since the data set is not collected from a single axis geometry.

Analysis of the 3D reconstructions employed a high-pass kernel for edge enhancement:

$$\begin{matrix} -1 & -1 & -1 \\ -1 & +9 & -1 \\ -1 & -1 & -1 \end{matrix}$$

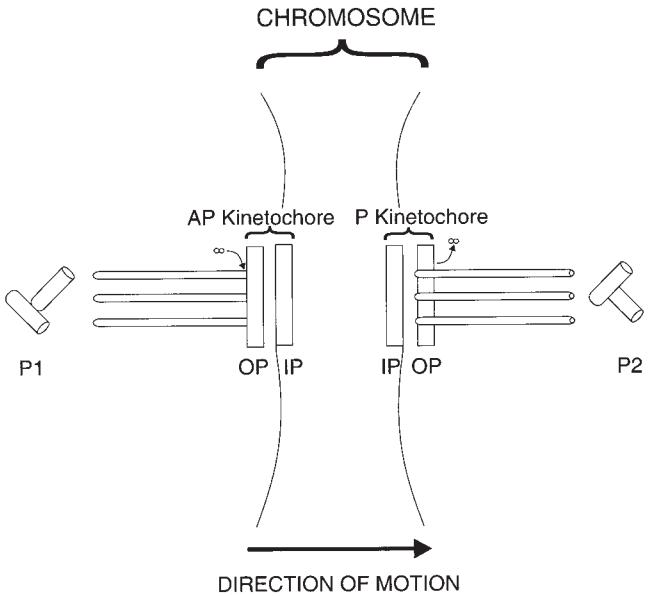

Figure 7. Illustration of a model for chromosome motion. The bi-oriented chromosome is moving toward the spindle pole designated P2. In this model, poleward motion involves removal of tubulin subunits from microtubules that are embedded in the P kinetochore outer plate (OP). These microtubules are postulated to be in contact with a force-generating mechanism that is located within the outer plate. Motion away from the other spindle pole (P1) is characterized by the addition of tubulin subunits onto microtubules at the surface of the AP kinetochore outer plate. Since microtubules at the surface of the outer plate are not in contact with the force generating mechanism, the AP kinetochore does not produce movement. The inner plates (IP) of the AP and P kinetochores are structurally distinct from the outer plates (OP) and separated by an intermediary space.

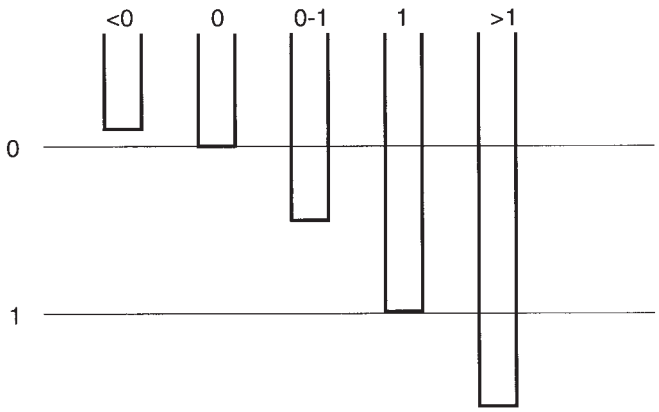

Figure 9. Illustration of the scheme used to assign relative penetration values to kinetochore microtubules. The boundaries of the outer plate are represented by values ranging from 0 to 1. Microtubules that have not penetrated the outer plate assume values < 0, microtubules that end within the outer plate assume values between 0 and 1, and microtubules that have penetrated through the outer plate into the space before the inner plate assume values > 1.

and a median filter for smoothing which applied a filter length of 9 and a box-shaped filter support.

III. ANALYSIS OF THE 3D RECONSTRUCTION

The 3D reconstructions were analyzed for relative kMt penetration into the kinetochore outer plate by quantitatively determining the relative positions of the kMts and the kinetochore outer plate, as illustrated in Figure 9. To facilitate comparisons of several kMts, the amount of penetration was defined as the ratio of the kinetochore plate width to the penetrating kMt length (Fig. 9). Positions at the boundaries of the outer plate were represented by values of 0 and 1, and therefore a kMt ending in the center of the plate was assigned a relative penetration value of 0.5. Any kMt that did not penetrate the outer kinetochore plate was characterized by a negative relative penetration value, while a kMt that passed through the proximal surface of the outer plate was characterized by a value > 1.

The implementation of these measurements was carried out using the Sterecon program for contour tracing [58]. In each slice of the volume, the borders of the kinetochore outer plate and the kMts were traced (Fig. 10). Tracing was aided by using a median filter to smooth the reconstruction and clarify the boundaries of the kinetochore outer plate (which are often difficult to distinguish from the interacting corona proteins) [Fig. 10(c)]. In a separate step, a high-pass kernel was applied for edge enhancement to facilitate identification of kMt ends [Fig. 10(b)]. Boundaries of the outer plate were drawn in every slice of the

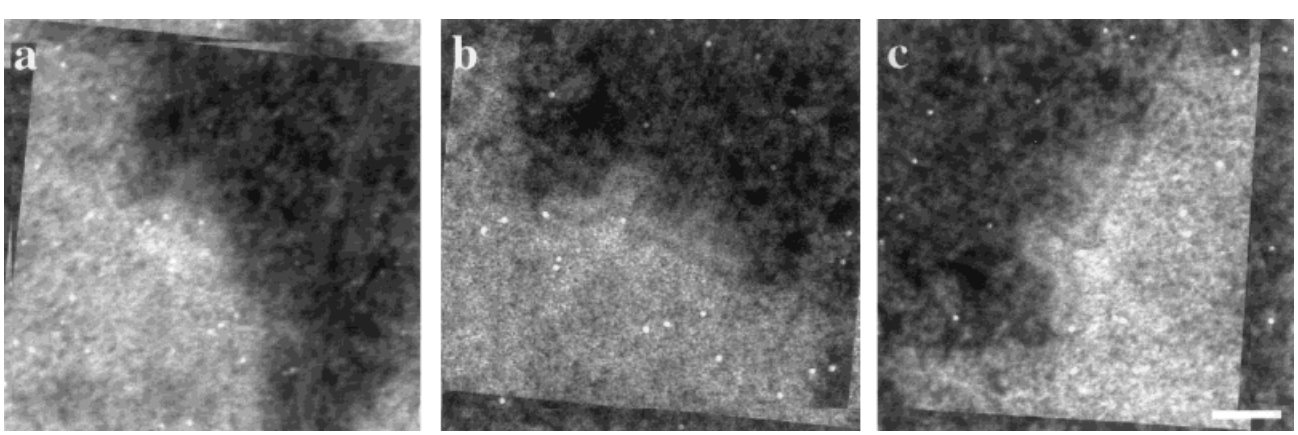

Figure 8. Digitized electron micrographs from the double-tilt series. The wrap-around effect in the images is the result of applying the alignment parameters. (a) View of the −60° tilt. (b) View of the 0° tilt. (c) View of the orthogonal 0° tilt. Bar = 0.25 μm.

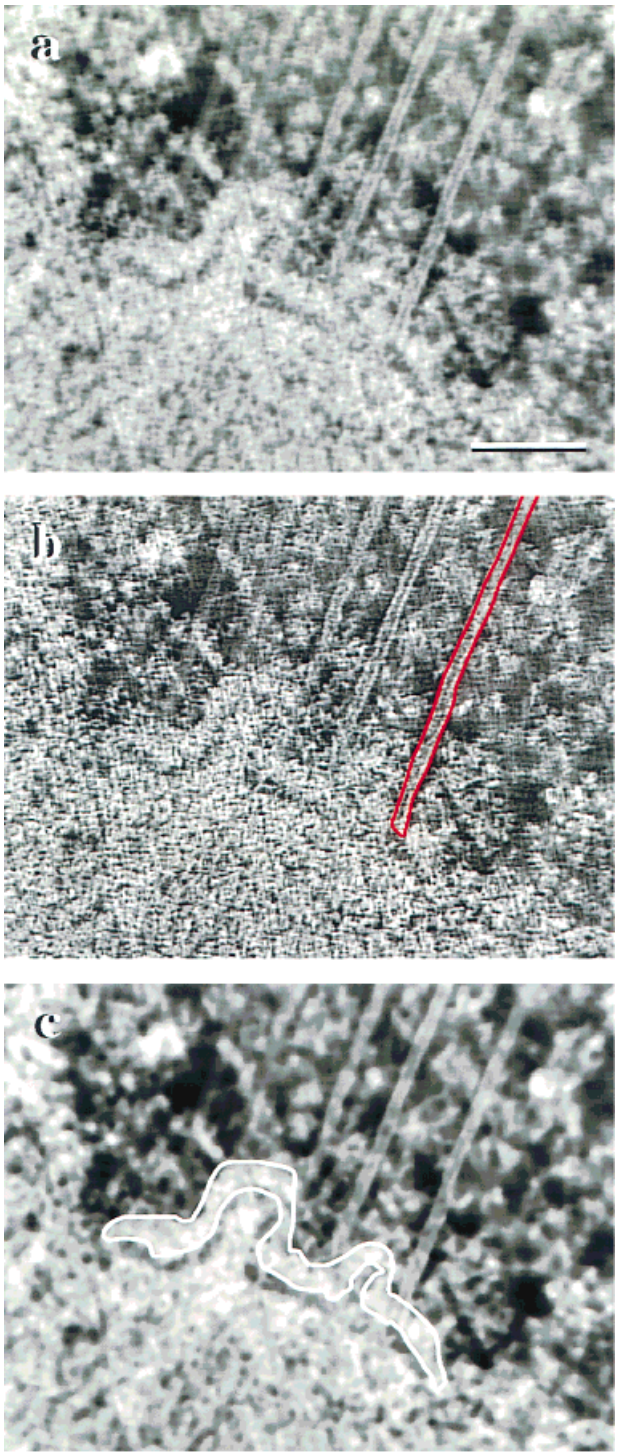

Figure 10. Determination of boundaries for the microtubules and the outer plate. (a) One slice of the tomographic 3D reconstruction volume of the kinetochore and its associated microtubules. (b) High-pass-filtered slice for Sterecon tracing of the microtubule (red). (c) Median-filtered slice for Sterecon tracing of the kinetochore outer plate (white). The one-pixel-wide Sterecon lines have been enhanced for viewing. Bar = 0.25 μm.

volume, while each kMt was independently traced in the central seven slices of that portion of the 3D reconstruction where the kMt appeared. Tracings of the outer plate and kMts were then displayed together in Sterecon (Fig. 11). Line measurements

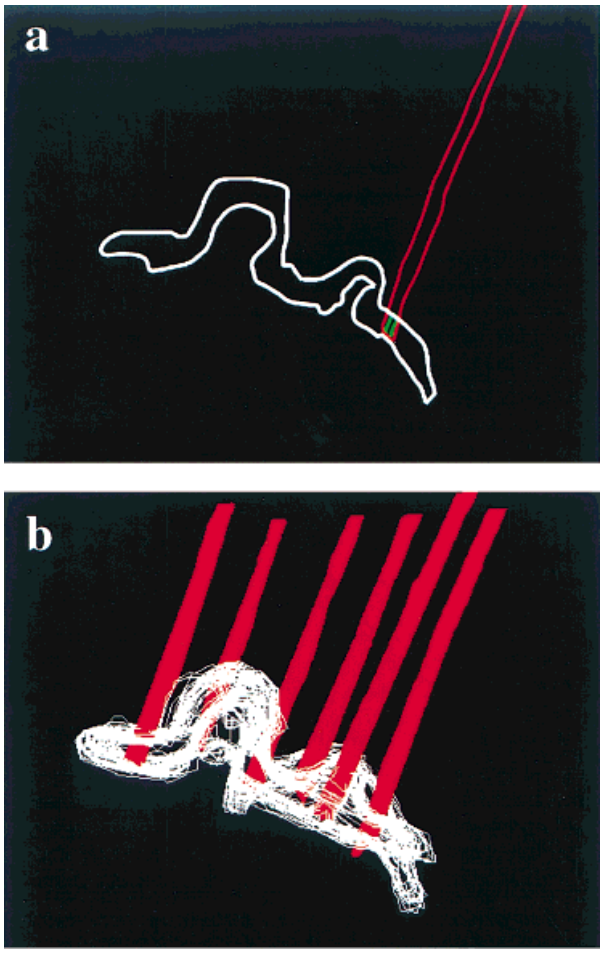

Figure 11. Determination of relative penetration. (a) Measurements of the outer plate width (green), and the microtubule penetration (also green), are made from the boundary information (Fig. 10) using the procedure described in the text. (b) Model of the 3D volume generated by stacking Sterecon tracings of each serial slice of the 3D reconstruction.

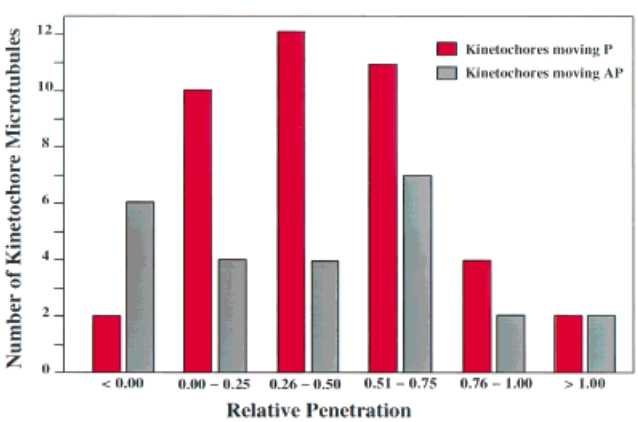

Figure 12. Distribution of the penetration of kinetochore-microtubules in the outer plate of AP kinetochores of congressing chromosomes and P and AP kinetochores of mono-oriented chromosomes. Relative penetration values are assigned to each microtubule according to the scheme in Figure 8 and as described in the text. In total, 25 kMts on AP kinetochores and 42 kMts on P kinetochores are represented in the distribution.

were drawn along the cylindrical axis of the kMt tracings, starting from the distal surface of outer plate and proceeding to the proximal surface of the outer plate (plate vectors) or to the end of the kMt [kMt vectors; see green lines in Fig. 11(a)]. The ratio of these vectors determined the relative penetration value as defined in Figure 9. When the kMt did not reach the distal surface of the outer plate, the kMt vector was negative, insuring that the relative penetration would be <0. In the example illustrated by Figures 10 and 11, the kMt terminated at the proximal surface of the outer plate; hence, the plate and kMt vectors were equal so the relative penetration was 1. For each kMt, measurements were averaged from the seven central slices that were traced.

IV. RESULTS AND DISCUSSION

The above procedure was used to determine the relative penetration of 42 kMts into the P kinetochores from five mono-oriented chromosomes, and 25 kMts into the AP kinetochores from five congressing and mono-oriented chromosomes. The resulting distributions of relative kMt penetration for AP and P kinetochores are presented in Figure 12. The distributions show no evidence of a correlation between direction of motion and relative kMt penetration. Preliminary data for P and AP kinetochores of bi-oriented chromosomes also show no evidence of a correlation between penetration and direction of motion (data not shown).

The results in Figure 12 are inconsistent both with the model in Figure 7 and with the earlier model postulating poleward force generation on the distal surface of the kinetochore outer plate [47]. Instead, the data indicate that the direction of chromosome motion is unrelated to the depth of kMt penetration, implying that the control mechanism operates via other parameters. The data also suggest that kinetochores move AP and P at roughly the same velocity as kMts grow and shrink; otherwise, a disparity in kMt penetration would arise owing to kMt growth and shrinkage pushing ahead of, or lagging behind, the kinetochores. Alternatively, it is possible that kMts grow and shrink at variable rates that are independent from the growth and shrinkage rates of other kMts on the same kinetochore.

Recent studies on artificially separated chromatids have demonstrated that a single kinetochore can bind to both spindle poles, and that individual kMts on the same kinetochore can move independently of one another [59]. This semi-independence of each kMt could explain why kMts on both AP and P kinetochores show a wide range of penetration levels (Fig. 12), but this still leaves open the question of how sufficient coordination is achieved so that all 24 kMts of an average metaphase kinetochore switch between growth and shrinkage with a change in the direction of chromosome motion. Furthermore, when chromatids are first separated by laser cutting, the AP kinetochore is ''paused'' and does not move for 20–90 s after separation [50]. Such a pause would be hard to achieve without some coordination in the direction of movement between individual kMts. Thus, it is unlikely that complete lack of coordination between kMts gives rise to the variable penetration levels seen in Figure 12.

Although unlikely, it is possible that differences in kMt penetration between AP and P kinetochores have been lost owing to specimen distortion during the chemical fixation and dehydration steps of the specimen preparation. We are currently investigating this possibility by preparing specimens using rapid freezing and freeze substitution [60,61]. This method provides superior structural preservation, but at present, there is no way to combine it with video light microscopy. Thus, the AP and P kinetochores cannot be identified with certainty in rapidly frozen, freeze-substituted preparations. For this reason, the data in Figure 12 are complementary to results obtained with freeze-substituted material and will be important in evaluating these future studies.

V. CONCLUSIONS

When used in conjunction with other experimental techniques, electron tomography is a powerful tool for addressing biological structure/function questions at the cellular level. For example, the data that we present in this report were obtained by combining electron tomography with video light microscopy, and were used to evaluate two models for the bidirectional motion of mitotic chromosomes. Other recent applications demonstrate that when adeptly applied, electron tomography can be used to address a wide variety of biological questions, including initiation of microtubule assembly from centrosomes, tension transmission in muscle contraction, initial events in mineralization of skeletal tissue, arrangement of nucleosomes in chromatin fibers, cristae structure in mitochondria, and secretion from the Golgi apparatus. Currently, new technical developments that reduce the deleterious effects of limited angular coverage and enable recording a tilt series with reduced electron dose are increasing the effectiveness of electron tomography. Employment of these methods will improve the quality of both the specimen preparation and the 3D reconstructions, and thereby extend and improve the analysis and interpretation that can be performed. Cryoelectron tomography is just beginning to find application, but it promises to open up exciting new frontiers for the exploration of biological structure in a native, hydrated state. In addition, rapid freezing can be used to capture transient functional states, and hence, cryoelectron tomography has the potential to explore a wide range of mechanistic questions. Thus, we can anticipate that in the near future, electron tomography will provide even more new insights into biological structure and function.

ACKNOWLEDGMENTS

The authors thank G. Cassels and Dr. M. Krioutchkova for assistance with video microscopy and specimen preparation, including ultra microtomy; as well as A. Pouchak for assistance with the 3D reconstructions and computer graphic measurements. They also thank Drs. M. Radermacher, P. Penczek, J. Frank, and A. Khodjakov for critical comments on the manuscript, and R. Cole, K. Buttle, and Drs. A. Khodjakov and C. Rieder for helpful advice and stimulating conversations during the course of this study. NIH Grant NCRRBTP P41-01219 partly supports the Wadsworth Center's Biological Microscopy and Image Reconstruction (BMIR) Facility as a National Biotechnological Resource. The video component of the BMIR Facility is also supported by the Wadsworth Center as a core facility.

REFERENCES

1. R. N. Bracewell. ''Strip integration in radio astronomy,'' *Aust. J. Phys.* **9,** 198–217 (1956).
2. R. N. Bracewell and A. C. Riddle. ''Inversion of fan-beam scans in radio astronomy,'' *Astrophys. J.* **150,** 427–434 (1967).
3. W. Hoppe. ''Dreidimensional abbildende Elektronenmikroskope.'' *Z. Naturforsch.* **27a,** 919–929 (1972).
4. D. DeRosier and A. Klug. ''Reconstruction of three-dimensional structures from electron micrographs,'' *Nature (London)* **217,** 130–134 (1968).
5. R. A. Crowther, D. J. DeRosier, and A. Klug. ''The reconstruction

of a three-dimensional structure from its projections and its application to electron microscopy,'' *Proc. R. Soc. London A.* **317,** 319–340 (1970b).
6. B. F. McEwen, ''Three-dimensional reconstructions of organelles and cellular processes,'' in *Electron Tomography.* J. Frank, Ed., Plenum Press, New York, 1992, pp. 281–311.
7. C. L. Woodcock, ''The organization of chromosomes and chromatin,'' in *Electron Tomography.* J. Frank, Ed., Plenum Press, New York, 1992, pp. 313–357.
8. J. Frank. ''Approaches to large-scale structures,'' *Curr. Opin. Struct. Biol.* **5,** 194–201 (1995).
9. M. Moritz, M. B. Braunfeld, J. W. Sedat, B. Alberts, and D. A. Agard. ''Microtubule nucleation by γ-tubulin-containing rings in the centrosome,'' *Nature* **378,** 638–640 (1995).
10. J. P. Schroeter, J.-P. Bretaudiere, R. L. Sass, and M. A. Goldstein. ''Three-dimensional structure of the *z* band in a normal mammalian skeletal muscle,'' *J. Cell Biol.* **133,** 571–583 (1996).
11. W. J. Landis, K. J. Hodgens, M. J. Song, J. Arena, S. Kiyonaga, M. Marko, C. Owen, and B. F. McEwen. ''Mineralization of collagen may occur on fibril surfaces: evidence from conventional and high-voltage electron microscopy and three-dimensional imaging,'' *J. Struct. Biol.* **117,** 24–35 (1996).
12. W. J. Landis, K. J. Hodgens, J. Arena, M. J. Song, and B. F. McEwen. ''Structural relations between collagen and mineral in bone as determined by high voltage electron microscopic tomography,'' *Microsc. Res. Technol.* **33,** 192–202 (1996).
13. R. A. Horowitz, D. A. Agard, J. W. Sedat, and C. L. Woodcock. ''The three-dimensional architecture of chromatin in situ: electron tomography reveals fibers composed of a continuously variable zig-zag nucleosomal ribbon,'' *J. Cell Biol.* **125,** 1–10 (1994).
14. C. L. Woodcock, S. A. Grigoryev, R. A. Horowitz, and N. Whitaker. ''A chromatin folding model that incorporates linker variability generates fibers resembling the native structures,'' *Proc. Natl. Acad. Sci. USA* **90,** 9021–9025 (1993).
15. P. W. Hawkes, ''The electron microscope as a structure projector,'' in *Electron Tomography.* J. Frank, Ed., Plenum Press, New York, 1992, pp. 17–38.
16. J. Zhu, P. Penczek, R. Schröder, and J. Frank. ''Three-dimensional reconstruction with CTF correction of the 70S *Escherichia coli* ribosome using energy-filtered cryo-electron microscopy,'' *J. Struct. Biol.* (in press).
17. R. Henderson. ''Image contrast in high resolution electron microscopy of biological macromolecules: TMC in ice,'' *Ultramicroscopy* **46,** 1–18 (1992).
18. M. Radermacher, ''Weighted back-projection methods,'' in *Electron Tomography.* J. Frank, Ed., Plenum Press, New York, 1992, pp. 91–115.
19. M. C. Lawrence. ''Alignment of images for three-dimensional reconstruction of non-periodic objects,'' *Proc. Electron Microsc. Soc. S. Afr.* **13,** 19–20 (1983).
20. M. C. Lawrence, ''Least-squares method of alignment using markers,'' in *Electron Tomography.* J. Frank, Ed., Plenum Press, New York, 1992, pp. 197–204.
21. J. Berriman, R. K. Bryan, R. Freeman, and K. R. Leonard. ''Methods for specimen thickness determination in electron microscopy,'' *Ultramicroscopy* **13,** 351–364 (1984).
22. P. Penczek, M. Marko, K. Buttle, and J. Frank. ''Double-tilt electron tomography.'' Appendix A: P. Penczek and R. Feuerbach, ''Marker alignment methods,'' *Ultramicroscopy* **60,** 393–410 (1995).
23. J. Frank and M. Radermacher, ''Three-dimensional reconstruction of non-periodic macromolecular assemblies from electron micrographs,'' in *Advanced Techniques in Biological Electron Microscopy.* J. Koehler, Ed., Springer-Verlag, Berlin, 1986, pp. 1–72.
24. J. Dubochet, M. Adrian, J.-J. Chang, J.-C. Homo, J. Lepault, A. W. McDowall, and P. Schultz. ''Cryo-electron microscopy of vitrified specimens,'' *Q. Rev. Biophys.* **21,** 129–288 (1988).
25. T. Ruiz, I. Erk, and J. Lepault. ''Electron cryo-microscopy of vitrified biological specimens: towards high spatial and temporal resolution,'' *Biol. Cell.* **80,** 203–210 (1994).
26. A. J. Koster, H. Chen, J. W. Sedat, and D. A. Agard. ''Automated microscopy for electron tomography,'' *Ultramicroscopy* **46,** 207–227 (1992).
27. A. J. Koster, M. B. Braunfeld, J. C. Fung, C. K. Abbey, K. F. Han, W. Liu, H. Chen, J. W. Sedat, and D. A. Agard. ''Towards automatic three dimensional imaging of large biological structures using intermediate voltage electron microscopy,'' *MSA Bull.* **23,** 176–188 (1993).
28. K. Dierksen, D. Typke, R. Hegerl, A. J. Koster, and W. Baumeister. ''Towards automatic electron tomography,'' *Ultramicroscopy* **40,** 71–87 (1992).
29. K. Dierksen, D. Typke, R. Hegerl, and W. Baumeister. ''Towards automatic electron tomography. II. Implementation of autofocus and low-dose procedures,'' *Ultramicroscopy* **49,** 109–120 (1993).
30. K. Dierksen, D. Typke, R. Hegerl, J. Walz, E. Sackmann, and W. Baumeister. ''Three-dimensional structure of lipid vesicles embedded in vitreous ice and investigated by automated electron tomography,'' *Biophys. J.* **68,** 1416–1422 (1995).
31. B. F. McEwen, K. H. Downing, and R. M. Glaeser. ''The relevance of dose-fractionation in tomography of radiation-sensitive specimens,'' *Ultramicroscopy* **60,** 357–373 (1995).
32. B. E. H. Saxberg and W. O. Saxton. ''Quantum noise in 2D projections and 3D reconstructions,'' *Ultramicroscopy* **6,** 85–90 (1981).
33. J. F. Conway, B. L. Trus, F. P. Booy, W. W. Newcomb, J. C. Brown, and A. C. Steven. ''The effects of radiation damage on the structure of frozen hydrated HSV-1 capsids,'' *J. Struct. Biol.* **111,** 222–233 (1994).
34. R. Hegerl and W. Hoppe. ''Influence of electron noise on three-dimensional image reconstruction,'' *Z. Naturforsch.* **31a,** 1717–1721 (1976).
35. D. P. Barnard, J. N. Turner, J. Frank, and B. F. McEwen. ''A 360° single-axis tilt stage for the high-voltage electron microscope,'' *J. Microsc.* **167,** 39–48 (1992).
36. C. L. Rieder. ''Formation of the astral mitotic spindle: Ultrastructural basis for the centrosome-kinetochore interaction,'' *Electron Microsc. Rev.* **3,** 269–300 (1990).
37. C. L. Rieder. ''The formation, structure, and composition of the mammalian kinetochore and kinetochore fiber,'' *Int. Rev. Cytol.* **79,** 1–58 (1982).
38. W. C. Earnshaw, ''Structure and molecular biology of the kinetochore,'' in *Microtubules.* J. Hyams, Ed., Wiley, New York, 1994, pp. 393–412.
39. A. F. Pluta, C. A. Cooke, and W. C. Earnshaw. ''Structure of the human centromere at metaphase,'' *TIBS* **15,** 181–185 (1990).
40. G. J. Gorbsky, P. J. Sammak, and G. G. Borisy. ''Chromosomes move poleward in anaphase along stationary microtubules that coordinate disassembly from their kinetochore ends,'' *J. Cell Biol.* **104,** 9–18 (1987).
41. A. A. Hyman and T. J. Mitchison. ''Modulation of microtubule stability by kinetochores in vitro,'' *J. Cell Biol.* **110,** 1607–1616 (1990).
42. R. B. Nicklas. ''The motor for poleward chromosome movement in anaphase is in or near the kinetochore,'' *J. Cell Biol.* **109,** 2245–2255 (1989).
43. R. U. Skibbens, V. Skeen, and E. D. Salmon. ''Directional instability of kinetochore motility during mitotic congression and segregation: A push-pull mechanism,'' *J. Cell Biol.* **122,** 859–875 (1993).
44. L. Cassimeris and E. D. Salmon. ''Kinetochore microtubules shorten by loss of subunits at the kinetochores of prometaphase chromosomes,'' *J. Cell Sci.* **98,** 151–158 (1991).
45. V. E. Centonze and G. Borisy. ''Pole-to-chromosome movements induced at metaphase: sites of microtubule disassembly,'' *J. Cell Sci.* **100,** 205–211 (1991).
46. T. Mitchison, L. Evans, E. Schulze, and M. Kirschner. ''Sites of microtubule assembly and disassembly in the mitotic spindle,'' *Cell* **45,** 515–527 (1986).

47. T. J. Mitchison. ''Microtubule dynamics and kinetochore function in mitosis,'' *Ann. Rev. Cell Biol.* **4,** 527–549 (1988).
48. L. Cassimeris, C. L. Rieder, and E. D. Salmon. ''Microtubule assembly and kinetochore directional instability in vertebrate monopolar spindles: Implications for the mechanism of chromosome congression,'' *J. Cell Sci.* **107,** 285–297 (1994).
49. C. L. Rieder and E. D. Salmon. ''Motile kinetochores and polar ejection forces dictate chromosome position on the vertebrate mitotic spindle,'' *J. Cell Biol.* **124,** 223–233 (1994).
50. A. Khodjakov and C. L. Rieder. ''Kinetochores moving away from their associated pole do not exert a significant pushing force on the chromosome,'' *J. Cell Biol.* **135,** 315–327 (1996) .
51. P. Huitorel and M. W. Kirschner. ''The polarity and stability of microtubule capture by the kinetochore,'' *J. Cell Biol.* **106,** 151–159 (1988).
52. T. J. Mitchison. ''Mitosis: Basic concepts,'' *Curr. Opin. Cell Biol.* **1,** 67–74 (1989).
53. J. C. Waters, R. V. Skibbens, and E. D. Salmon. ''Oscillating mitotic newt lung cell kinetochores are, on average, under tension and rarely push,'' *J. Cell Sci.* **109,** 2823–2831 (1996).
54. C. L. Rieder and S. P. Alexander. ''Kinetochores are transported poleward along a single astral microtubule during chromosome attachment to the spindle in newt lung cells,'' *J. Cell Biol.* **110,** 81–95 (1990).
55. C. L. Rieder and R. W. Cole, ''Perfusion chambers for high-resolution video light microscopic studies of vertebrate cell monolayers: some considerations and a design,'' in *Methods in Cell Biology: Video Microscopy*. G. Sluder and D. E. Wolf, Eds., Academic Press, New York (in press).
56. U.-P. Roos. ''Light and electron microscopy of rat kangaroo cells in mitosis. II. Kinetochore structure and function,'' *Chromosoma (Berlin)* **41,** 195–220 (1973).
57. J. Frank, M. Radermacher, P. Penczek, J. Zhu, Y. Li, M. Ladjadj, and A. Leith. ''SPIDER and WEB: Processing and visualization of images in 3D electron microscopy and related fields,'' *J. Struct. Biol.* **116,** 190–199 (1996).
58. M. Marko and A. Leith. ''Sterecon-three-dimensional reconstructions from stereoscopic contouring,'' *J. Struct. Biol.* **116,** 93–98 (1996).
59. A. Khodjakov, R. W. Cole, B. F. McEwen, K. F. Buttle, and C. L. Rieder. ''Chromosome fragments possessing only one kinetochore can congress to the spindle equator,'' *J. Cell Biol.* **136,** 229–240 (1997).
60. J. C. Gilkey and L. A. Staehelin. ''Advances in ultra rapid freezing for the preservation of cellular ultrastructure,'' *J. Electron Microsc. Technol.* **3,** 177–210 (1986).
61. S. Hippe-Sanwald. ''Impact of freeze substitution on biological electron microscopy,'' *Microsc. Res. Technol.* **24,** 400–422 (1993).
62. G. A. Meek, *Practical Electron Microscopy for Biologists* (Wiley, London), 1976.
63. M. Radermacher. *Dreidimensionale Rekonstruktion bei kegelförmiger Kippung in Elektronenmikroskop,* thesis, Technical University, Munich, 1980.